Estimation of surface topography and wear loss of laser metal deposited Ti6Al4V and Cu

Dr Mutiu F. Erinosho[*]*, Prof Esther T. Akinlabi*

[*] *Department of Mechanical Engineering Science, University of Johannesburg, Auckland Park Kingsway Campus, Johannesburg, 2006, South Africa.*

E-mail: mferinosho@uj.ac.za or mutiuerinosho@yahoo.com

Abstract

The atomic force microscopy (AFM) analysis is a process that involves the detailed analyses of the surface of a three dimensional sample piece. A good image is always generated on such a sample once the settings are implemented correctly. And as such, the amplitude set point played a vital role in achieving a better image. For surface engineering applications, a small proportion of Cu has been added to Ti6Al4V alloy and deposited using a 2kW Ytterbium Fibre Laser. This paper presents the evolving microstructures and the surface topographies of the laser deposited Ti6Al4V/Cu alloys. The formation and the output of the microstructure depend on the laser processing parameters employed. The α-Ti lamella formed was observed to gain coarseness with respect to the increase in the laser power. The migration of the β-phase has been impeded during solidification due to the low strain hardening effect posed by the α-Ti lamella thereby limiting the further dislocation of the β-phase within the crystal structure. A clear picture of the height, amplitude and the phase shift of the scanned sample were viewed before a capture can be made. A correlation between wear loss and surface roughness has been established among the laser deposited samples.

Keyword: *laser metal deposition, microstructure, surface roughness topography, wear loss, Ti6Al4V/Cu alloy*

1. Introduction

Nowadays, the use of metallic powder is an advanced manufacturing technology for producing a wide range of finished and semi-finished engineering components. It is used in the repair of parts that are difficult to machine. Powder metallurgy can be used for processing various kinds of metal and alloys in the near-net shape form.[1] Most of these powders are processed using various laser techniques such as laser metal deposition, laser sintering and selective laser melting (SLM). The SLM is a powder bed fusion process in additive manufacturing that uses a 3D CAD model or rapid prototyping that uses high power-density laser to melt and fuse metallic powders into solids.[2] It is an advanced manufacturing method which can control the mechanical properties and microstructural behaviour of characterized samples with different process parameters.[3] This has gained interest in the manufacturing of engineering parts in the field of aerospace, oil and gas, medicals; thereby improving the production cycle, complex geometry, the buy-to-fly ratio and optimal material's usage thereby saving costs.[4] The additive manufacturing allows the direct fabrication of functional parts with complex shapes from digital models.[5] The laser exhibits unique and distinctive features including monochromatic wavelength, coherency, temporal nature and an irradiance beam profile.[6] The Ti6Al4V alloy is desirable in the aerospace, chemical industries, marine, energy, medical and the automotive industrial services since it exhibits a combination of mechanical, physical and corrosion- resistance properties.[7-10] This alloy has been modified with different other elements in the literature depending on the application, and the mechanical properties have been reportedly improved.[11-15] Atomic force microscopy (AFM) is a process that involves the full focus-ness of the surface of a three dimensional object. The method can be applied to soft and hard synthetic materials as well as microbiology

structures such as cells and tissues regardless of their opacity or conductivity.[16] The surface morphology of Inconel 825 with multi wall carbon nano tube after an electrical discharge machining process was investigated using the AFM analysis[17]; it was observed that the specimens ignited with the carbon nano tube have excellent surface finish and morphology as compared with the samples without the carbon nano tube. The AFM 3D topography analyses of Ti6Al4V and γ-TiAl alloys were studied after different plasmo-chemical modifications for biomedical application [18] and the authors found that Ti6Al4V alloy treated with plasmo-chemical exhibited low cytotoxicity and the surface roughness values of all the modified γ-TiAl alloys were also reported to decrease. Surface roughness is an important aspect of product quality that intensely affects the performance of mechanical parts and the production costs. The effects of laser surface remelting on the morphology of Al–Fe alloys were scrutinized before and after surface treatments for a tailored aerospace application. The presence of homogenous structure, lamella stacking structure and the dominating metastable Al_2O_3 of 1.5 weight percent of Fe alloy were reported to contribute to an increase in the hardness value of the laser-treated sample compared to the untreated sample.[19] According to the hand book of structural alloys, most of these alloys, especially the titanium alloys have found constrained use in the mechanical engineering applications due to their poor abrasive wear resistance, high coefficient of friction and the fretting characteristics. These irregularities behaviours of the alloys could be modified by treating the surfaces with coatings.[20] Four main mechanisms have been postulated to improve the wear behaviour of titanium alloys and these are: increase in the surface roughness, increase in the hardness, inducing compressive residual stress, and reduction in the coefficient of friction.[21]

As far as the authors know, there is no reported literature on the surface topography analysis and evaluation of titanium alloy grade 5 and copper for marine application to control degradation of locomotive parts immersed in sea water which is caused by microorganism. This work therefore presents the microstructural characterizations, the surface roughness topography of laser metal

deposited Ti6Al4V and Cu alloys using the AFM technique, and the wear loss. Due to the height of both the clad and the substrate, a careful roughness analysis was conducted on the surface of the single-track layered deposited samples. The laser power, the scanning speed, the powder flow rate and the gas flow rate respectively were put into consideration for the deposition process whilst the height, the amplitude and the phase shift of the samples under the AFM probe were measured and captured. A correlation between the surface roughness and wear loss was also investigated.

2. Materials and Methods

The laser deposition process was conducted on a 2 kW Ytterbium Fibre laser system at the National Laser Centre, Council for Scientific and Industrial Research (NLC-CSIR), Pretoria, South Africa. The system has a wavelength of 1.047 μm and works interrelated with a Kuka robot. A three way nozzle through which the powders and laser pass is attached to the end of the robot.

The powders used for this research work are Ti6Al4V alloy and Cu powders. The Ti6Al4V alloy powder was supplied by F.J. Brodmann and Co., L.L.C., Louisiana, TLS Technik GmbH, Germany. The Cu powder was supplied by the Industrial Analytical (Pty) Limited, South Africa. The two powders were poured into two separate cleaned cylindrical hoppers.

Tables 1 and 2 show the chemical composition of the Ti6Al4V alloy and the Cu powders.

Table 1. Chemical composition of the Ti6Al4V powder

Element	Al	V	Fe	C	N_2	H_2	O_2	Ti
Wt.%	6.30	3.90	0.17	0.008	0.005	0.005	0.140	Balance

Table 2. Chemical analysis of Cu powder

Powder	Percentage (%)	Hydrogen loss (%)	Apparent density (g/cm^3)
Cu powder	99.83	0.31	5.1

The powders were fed from the two cylindrical hoppers and flow out through a three way nozzle on to the substrate during deposition.

Table 3 shows the experimental matrix used in this present study.

Table 3. Experimental matrix

Sample Name	Laser Power (W)	Scanning Speed (m/min)	Powder Flow rate (g/min)		Gas Flow rate (l/min)	
			Ti6Al4V	Cu	Ti6Al4V	Cu
P27	1600	0.3	4.175	0.32	3	1
P35	1200	0.3	4.008	0.32	3	1
P36	1400	0.3	4.008	0.32	3	1
P37	1600	0.3	4.008	0.32	3	1

The sample designated by P27 represents deposition with 3 weight percent of Cu (Ti6Al4V/3Cu alloy) while the samples from P35 to P37 designate deposition with 5 weight percent of Cu (Ti6Al4V/5Cu alloy) respectively. The powder hopper was calibrated in revolutions per minute. The flow rates of the powders were measured in gram per minute (g/min). Six consecutive measurements were made for each powder for every 1 minute and weighed. The average was calculated for each powder to know the g/min.

The material used for the parent material (substrate) was 99.6 % solid Ti6Al4V alloy; and it was supplied by Titanium Metal, 12215 Kirkham Road, Poway, United States. The substrate was produced by a rolled mechanism, and then cut into plates of 102 X 102 X 7.45 mm^3 dimensions. Prior to laser-powder deposition, the substrate was grit-blasted in the compartment of a sand-blasting machine to prepare the surface for firm metallographic bonding, and to allow for the removal of contaminants on

the surface of the substrate. The blasted plate was then cleaned with acetone, rinsed under running water, and dried off with a hand dryer. The cross sections of the samples were mounted in poly fast prior to further characterization.

2.1. Microstructure

The samples were ground (plain and fine grinding), polished and etched according to E3-11 ASTM standard guide for preparation of metallographic specimens [22]. Prior to microscopic observation, the Kroll's reagent was prepared for the etchant (100 ml H_2O, 2-3 ml HF and 4-6 ml HNO_3) respectively. Each sample was etched for 15 seconds. The microstructures of the laser deposited samples were observed under the BX51M Olympus microscope at low and high magnifications. The SEM analysis was carried out on the Ti6Al4V and Cu powders. The particle size analyses of the two powders were conducted on a Microtrac Tri-laser System. The system is a blue-wave S3500 particle size analyser equipped with a three-laser system, which performs the analyses. The system is sensitive in distributing the particle sizes. A light-scattering measurement is adopted with the system; and it combines the three lasers and the two detector arrays in a fixed position. The particle size analysis was conducted, according to E2651-13 ASTM standard [23].

2.2. Surface Roughness Topography Using the AFM

The di3000 Atomic Force Microscope at the Microscopy and Microanalysis Unit, Department of Biology, University of Witwatersrand, South Africa, was used to evaluate the surfaces of the composites. The AFM is a surface-imaging system that employs a micro-fabricated mechanical tip under a probe cartridge, having a high resolution, as the primary probe for analyzing the physical properties of the surface. Before operating the AFM instrument and mounting the samples on the rotary table, the system is switched ON by following the manual. Each sample was scanned under a probe cartridge attached with a silicon cantilever. The height, the amplitude and the phase shift of the samples

are measured. The operation mode is always set to Tapping Mode in order to remove frictional forces by surface contact and to prevent the breakage of the tip. The cantilever tip was finally engaged to the samples, after setting the appropriate parameters.

2.3.1. Dry Sliding Wear Test

A dry sliding wear tests were conducted on a micro tribometer module, CETR UTM-2 operating with linear reciprocating motion drive. A load of 25 N, stroke length of 2 mm, oscillation frequency of 5 Hz and test duration of 1000 seconds were selected for the process. 9.5 mm diameter tungsten carbide ball was made to rub against the moving samples. The dry sliding wear tests were carried out according to the ASTM G133-05 for determining the sliding wear of metals [24]. The wear losses were calculated from the length of the stroke, the width of the wear scar and the depth of wear. These are indicated in equations (1) and (2) [25].

$$W_l = L_k \left[R_p^2 sin^{-1}\left(\frac{W}{2R_p}\right) - \frac{W}{2}\left(R_p - W_d\right)\right] + \frac{\pi}{3} W_d^2 \left(3R_p - W_d\right) \quad (1)$$

$$W_{dt} = R_p - \sqrt{R_p^2 - \frac{W^2}{4}} \quad (2)$$

Where W_l is the wear loss; L_k is the stroke length; R_p is the pitch radius; W is width of the wear scar and W_{dt} represents the wear depth.

3. Results and Discussion

3.1. Microstructural Evaluation

Figure 1 (a) and (b) show the morphologies and the particle size distributions of Ti6Al4V and Cu powders.

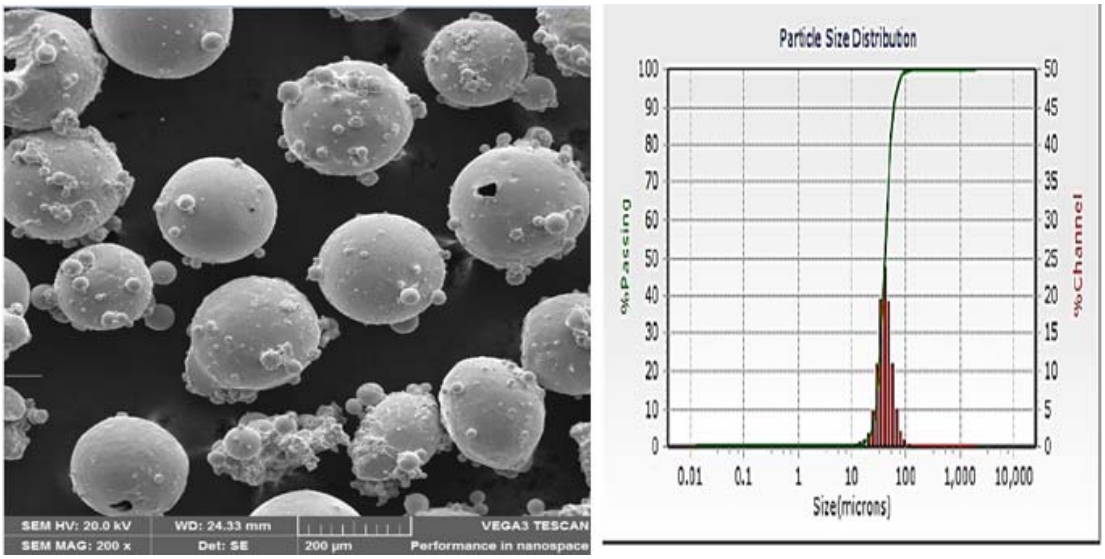

(a)

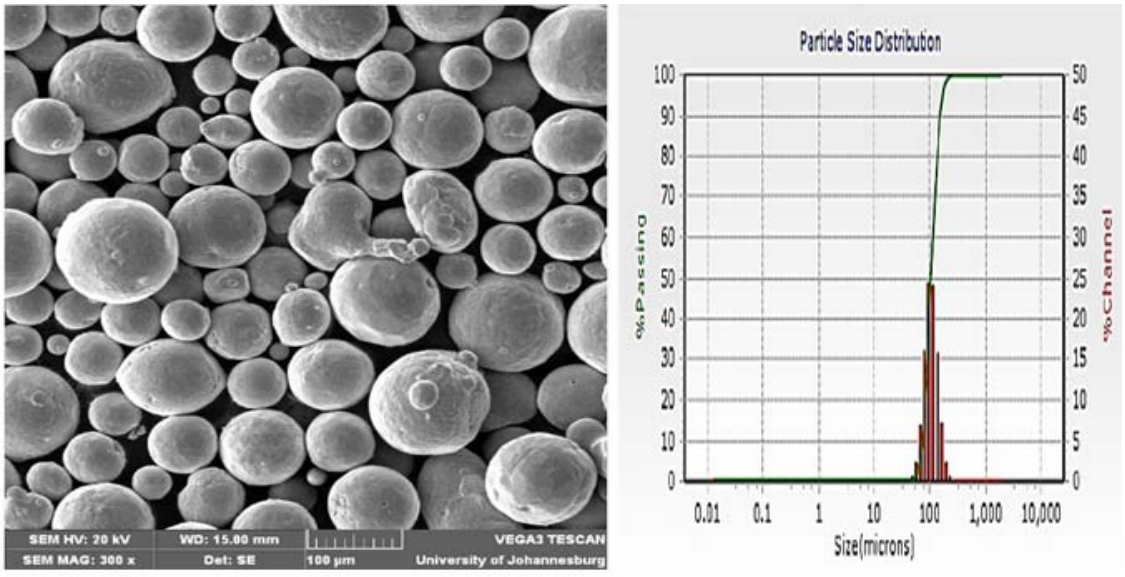

(b)

Figure 1. SEM morphologies and particle size analysis and distribution (a) Ti6Al4V powder; (b) Cu powder

The morphologies of both the Ti6Al4V and Cu powders were spherical in shape. The particle size of Ti6Al4V was observed to be equiaxed and the surfaces were smooth with satellites (dust particles) agglomerated scantily to the bigger particles. The particle sizes of Cu were also observed to be equiaxed in morphology and showed denser faces compared to the Ti6Al4V alloy powders. The particle size analyses of the Ti6Al4V alloy and the Cu powders were furthermore presented. The plots of the percentage of passes and channels against the particle size result in the distribution and analysis of the powder particle sizes. In the particle size distribution of Ti6Al4V alloy powders, as observed in Figure 1 (a), the highest percentage of channels lie between 70 µm and 80 µm. Some of the particle sizes are in the range less than 70 µm, while others are in the range of 70 µm to 120 µm. The main particle size distribution of Cu powders as presented in Figure 1 (b) lies between 100 µm and 300 µm of the percentage of channels.

The X-ray diffraction was conducted on the Ti6Al4V alloy and the Cu powders, in order to identify the phases present. Figures 2 (a) and (b) show the diffractogram of the Ti6Al4V alloy and Cu powders. A K-beta filter with 40 kV and 40 mA set-up was used. The scanning mode is continuous and in the range between 3^{o} to 90^{o}.

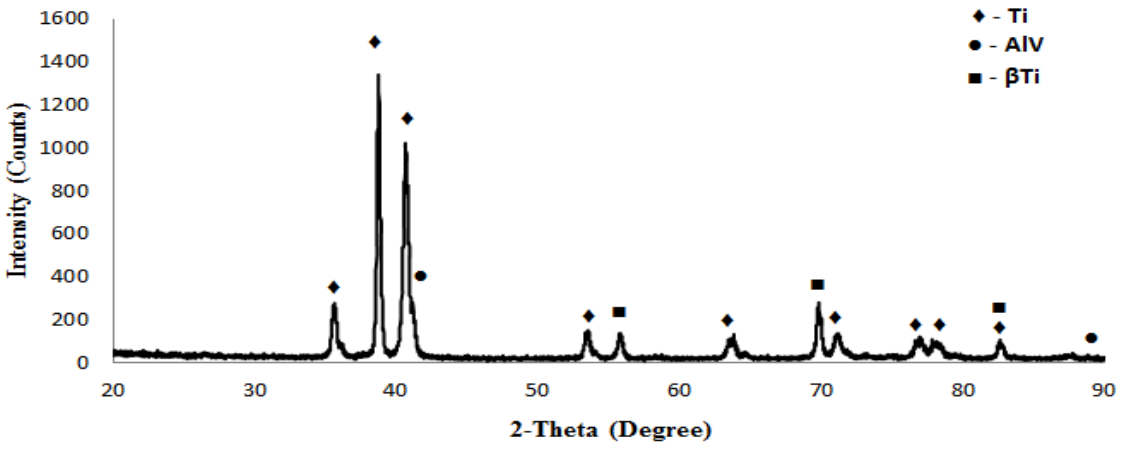

(a)

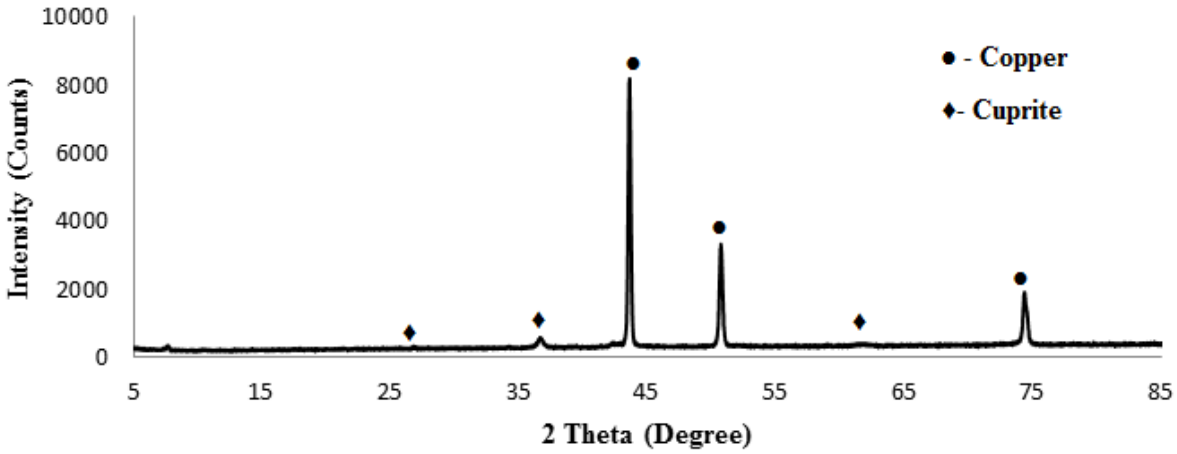

(b)

Figure 2. XRD analyses of the powders (a) Ti6Al4V alloy (b) Cu

From the quantitative analysis of Figure 2 (a), Ti is the major element in the constituent, having the highest peak of 54.2 % and a lattice strain of about 0.167 %. The two major peaks of Ti are very narrow and observed at $2\Theta = 38^{o}$ and 42^{o} – while other Ti peaks were observed towards increasing 2Θ, but with low peaks. The quantitative analysis results of Figure 2 (b) show that Cu is the major phase within the spectra; and it was almost 90 % in content. The Cu peaks were identified at $2\Theta = 44^{o}$, 52.3^{o} and 75^{o}. The cuprite (Cu_2O) peaks were found to be mere traces.

The results of the XRD analyses with the identification of the phases present in Ti6Al4V and Ti6Al4V/Cu alloys are presented. Figure 3 describes the XRD spectra and the phases, as well as the compositions of Ti6Al4V, Ti6Al4V/3Cu and Ti6Al4V/5Cu alloys.

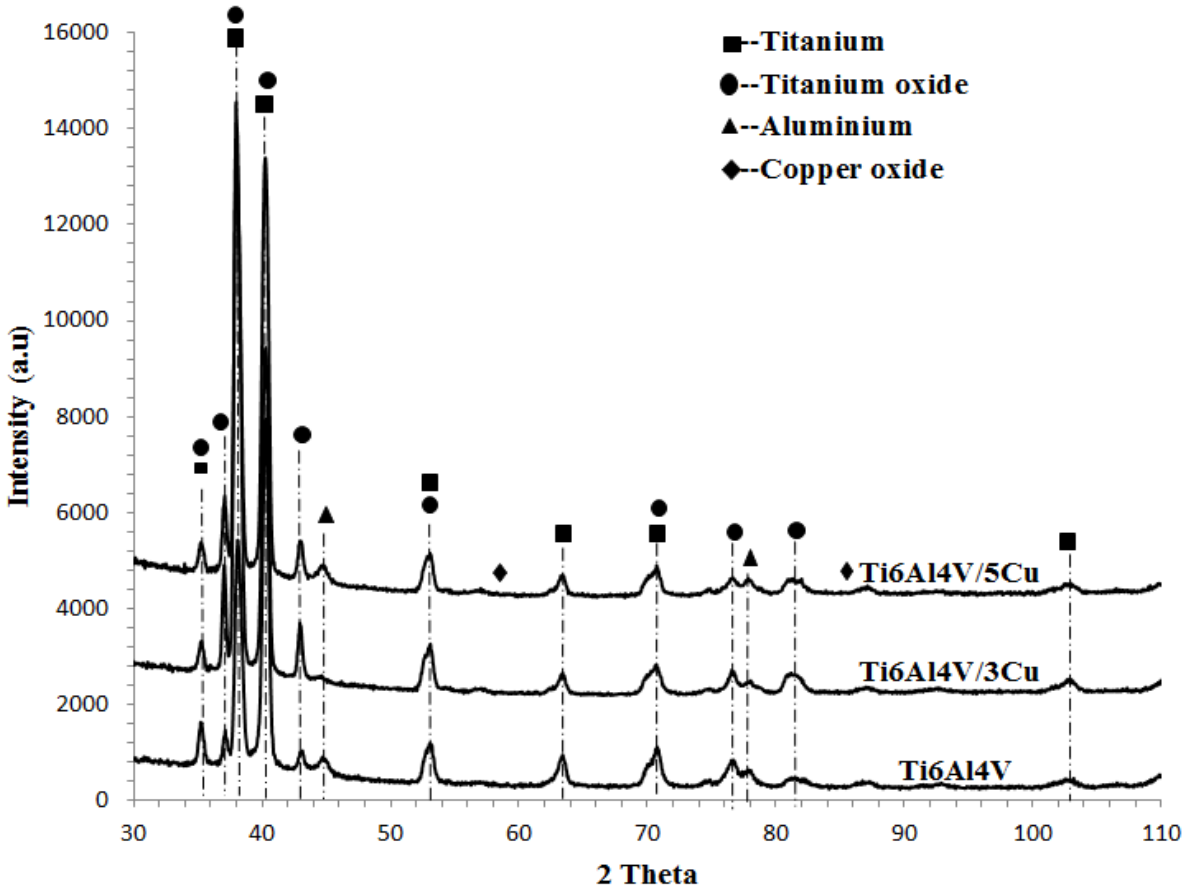

Figure 3. XRD spectra and phase compositions of Ti6Al4V, Ti6Al4V/3Cu and Ti6Al4V/5Cu alloys

The recording range 2 theta (2Θ) for the XRD test is between 30º and 110º under a target tube of Cu. It can be observed that the phases for Ti6Al4V, Ti6Al4V/3Cu and Ti6Al4V/5Cu alloys are similar in trend; but the peaks are different at the most noticeable phases between 35º and 45º. The peaks are very narrow and display sharp edges. The major hexagonal titanium (Ti) peaks are observed at 2Θ = 35.5º, 38.5º, 40º, 53º, 63.5º, and 71º, respectively. At 2Θ = 38.5º and 40º, the peaks of Ti for Ti6Al4V alloy are much lower than the peaks for Ti6Al4V/3Cu and Ti6Al4V/5Cu alloys, respectively. The peak of Ti6Al4V alloy is observed to be lower than those of the Ti6Al4V/3Cu and Ti6Al4V/5Cu alloys. The peak for Ti6Al4V/3Cu alloy is a bit higher than the Ti6Al4V/5Cu alloy. The hexagonal TiO peaks are more pronounced and exhibit the highest peak at 2Θ = 40º. Low peaks of Al were also identified at 2Θ

= 46° and 78°. With the peaks observed, especially at the most noticeable peaks, it can be deduced that the presence of Cu in the clad initiated the formation of more oxides of Ti which promote the formation of accumulated protective films over the surfaces of the Ti6Al4V/Cu alloys.

Figures 4 (a) to (d) show the microstructures of the laser deposited Ti6Al4V/Cu samples. The Figures represent the microstructures of the etched Ti6Al4V/Cu alloys of samples P27, P35, P36 and P37 respectively.

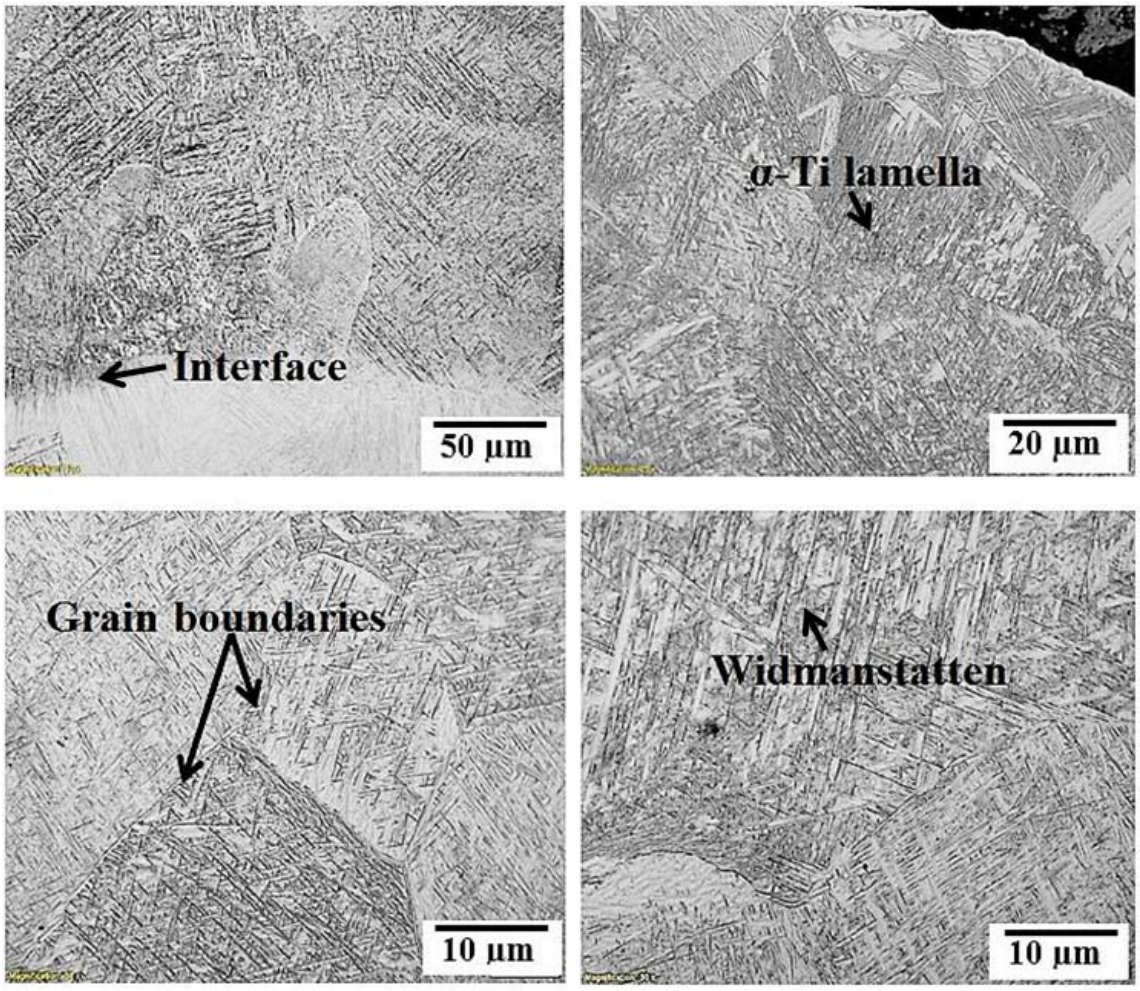

Figure 4. Microstructures of the laser deposited samples: (a) Sample P27-Ti6Al4V/3Cu: 1600 W and 0.3m/min; (b) Sample P35- Ti6Al4V/5Cu: 1200 W and 0.3m/min; (c) Sample P36- Ti6Al4V/5Cu: 1400 W and 0.3m/min; (d) Sample P37- Ti6Al4V/5Cu: 1600 W and 0.3m/min.

From samples P35 to P37, the laser powers varied between 1200 W and 1600 W. The powder flow rates of 4.008 g/min for Ti6Al4V and 0.32 g/min for Cu were kept constant. The effect of the laser power has been studied on the microstructures of samples P35 to P37 of Ti6Al4V/5Cu alloys. Coarse basket weave (Widmanstätten) microstructures were unevenly dominated towards the top of the deposit. The effect of the laser beam affects the top of the deposit compared to the middle and the interface of the alloy. The basket weave-like reduced in their robustness towards the fusion zone due to the heat input sinking effect and becomes thinner and fused towards to the fusion zone and the heat affected zone. It was observed that the energy density and the melt pool increases as the laser power increases. This in turn made the α-Ti lamella to gain their coarseness. The α-Ti phases were also found obstructing the migration of the β-phase due to the low strain hardening thereby limiting the deformation and the dislocation of the β-phase within the crystal structure during solidification. At higher laser power, the time required to cool is high. The Widmanstätten microstructures toward the fusion zone are fused and added to the bond strength that exists between the clad and the substrate's interface [26]. At lower energy density, the cooling rate was fast during the deposition and result in a greater number of nuclei within the lattice structure [27]. The powder flow rate used during deposition can also contribute to the granularity of the microstructure [28]. The quality of the deposition depends on how the powder particles are deposited into the melt pool [29], and a higher powder flow rate can cause an increase in the nucleation density of the melt pool [30]. With the laser powers used in this experiment, the powders were fully melted and due to the 3 wt % and 5 wt % of Cu used, the melting behaviour was not observed. The melting point of titanium alloy is about 63.5% more than that of Cu. And as such, the little Wt % Cu in the Ti6Al4V alloy lattice were fully melted under the high laser powers used since the specific heat capacity of the Cu introduced is 0.385 $Jg^{-1}k^{-1}$ which is about 37 % less than that of Ti6Al4V alloy. However, there were no intermetallics formed due to the low percentage of Cu used. The little percentage used only improved the mechanical properties to some extent. The increase in the laser power tends to create more melt pool and the heat input generated is

also increased thereby widen the heat affected zone. The morphology of the α-Ti phase can appear as equiaxed or acicular depending on the cooling rate and as such can lead to different features in the microstructures of the α-phase with different mechanical properties. As such, the effect stimulates the ductility of the alloy; since the cooling rate is at a slow bound, as a result of the high laser power. The different microstructural behaviour is much reliant on the laser power, the heat input and the interaction time.

3.2. Surface Topography Analyses

This section highlights the surface topography results of the laser metal deposited samples (sample P27, sample P35, sample P36, and sample P37, respectively) characterized on the AFM equipment. Figures 5 (a) to (c) show the 3D view of the surface topography and the 2D view of the height and the amplitude of sample P27 of Ti6Al4V/3Cu alloy.

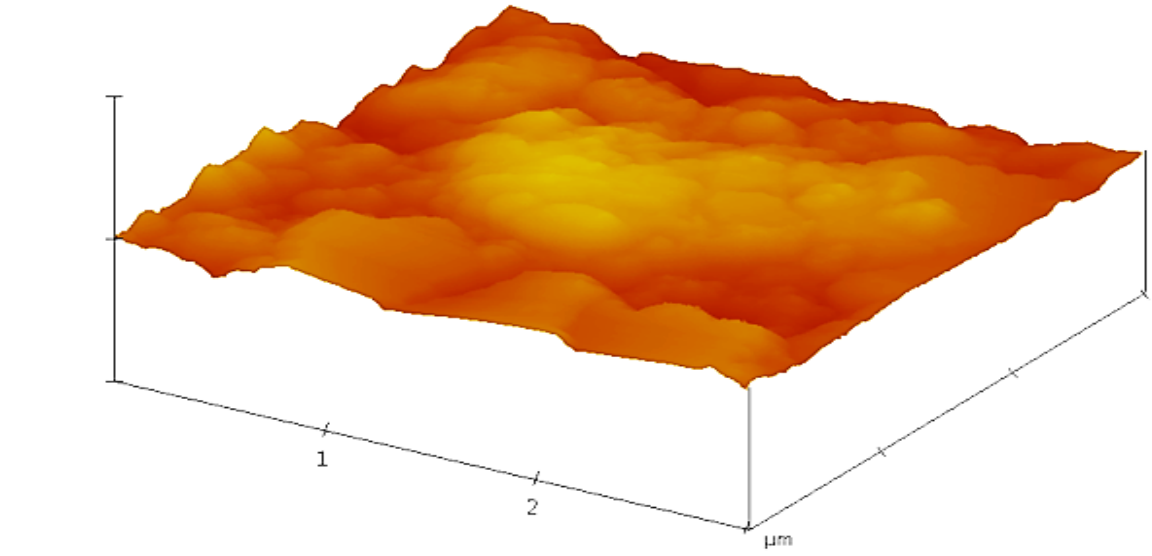

(a)

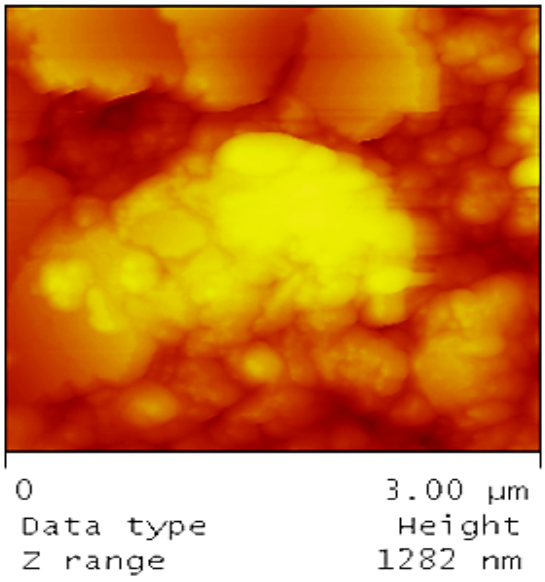

(b)

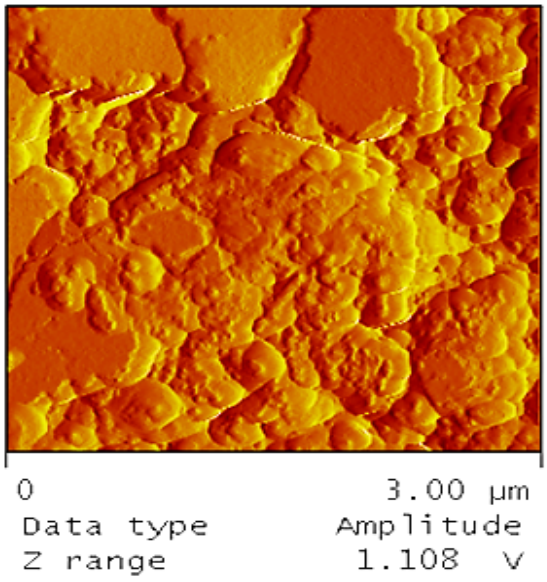

(c)

Figure 5. Surface topographies of the laser deposited Ti6Al4V/Cu alloys showing the 3D view and the 2D views of the height and the amplitude for sample P27

From the 2D view of the height observed, the colours are represented to show the high, medium and low settings of the legend representing the surface. Haugstad [16] reported that the multi-colour images of surface topography are mainly for viewing purposes. The height of the surface is determined when the probe (sharp tip) under the flexible cantilever touches the surface. Thus, the vertical Z displacement can be measured through the feedback sensor. The tip-sample interaction remains approximately constant; and the vertical tip movement is scanned to get the XY image [16]. A clearer image is viewed when the topography is not too rough. At times, when the tip scans through the valley of the sample, no image is observed; and the Z position is retracted on the Trace Scope (a good and commendable trace scope is observed in Figure 5). All the surface topographies of the participating samples have ridges (crests) and valleys. Sample P27 of Ti6Al4V/3Cu alloy shows some table crests in the 2D view of the amplitude, as shown in Figure 5 (c). For sample P27, the scan size of 3 μm and the scan rate of 1 Hz were installed to view the image. The X and Y positions were engaged at -19783.4 μm and -42151.3 μm, respectively for all the samples. The Z-Range obtained for the height and the amplitude, as shown in the 2D view of Figures 5 (b) and (c) are 1282 nm and 1.108 V. For sample P35 of Ti6Al4V/5Cu alloy, the scan size of 3 μm and the scan rate of 1 Hz were also installed to view the image. The Z-Range obtained for the height and the amplitude are 744.9 nm and 0.9749 V. Scan size of 2.5 μm and scan rate of 0.5 Hz were installed to view the sample P36 alloy and the Z-Range obtained for the height and the amplitude are 400 nm and 0.5 V. Good image was observed for sample P36, although the scan size and scan rate used were slightly lower compared to the rate at which other samples were scanned due to poor image observed. The scan size selected for viewing a good image on a sample might not be the same for another sample, because of the inconsistencies in the laser sample's surface topographies and the variation of parameters during laser deposition. A scan size of 4 μm and a scan rate of 1 Hz were used to view the image of sample P37. The Z-Range obtained for the height and the amplitude are 630.5 nm and 0.5721 V. In viewing all the samples, the amplitude set point played a vital role in getting a better image. Both the images and the scope trace are also very important in determining a

clearer image. However, the measurement of meaningful values of roughness factor depends on the instrument settings such as the scan size and resolution [33]. Once any parameter is altered, both the image and the scope trace must be checked to view the status of the surface topography. Although, it is very difficult to get a perfect topography and once a good image appears, capture is needed to be taken. There is no specific approach that yields the true surface area for microscopically rough surfaces. Thus, comprehensive picture of a surface is not possible due to limitations of the instrument and the discrete character [34].

Figure 6 shows the roughness particle analysis of sample P27. This shows the bearing area in percentage and the particle scan depth.

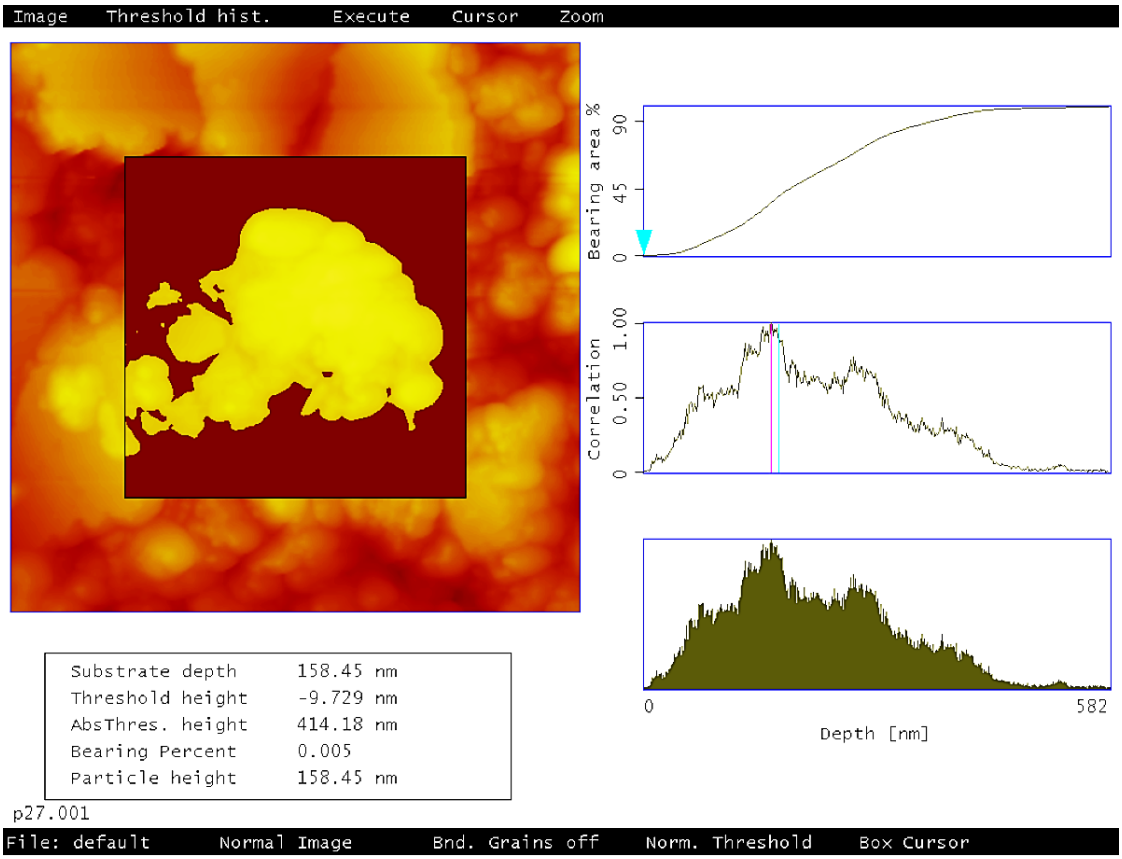

Figure 6. Roughness particle trend and bearing area of sample P27 deposited at a laser power of 1600 W.

The roughness particle height and the substrate depth of samples P27, P35, P36 and P37 are 158.45 nm, 144.11 nm, 82.577 nm and 114.11 nm respectively while the bearing area percentages of 0.005 %, 0.002 %, 0.001 % and 0.005 % in the Abbort firestone or bearing curve are measured. These values give the textures of the surface. The curve is the integral of the amplitude distribution function from above the surface to the height of interest [31]. The maximum peak as observed from the correlation axis gives the probability density. The squared region in Figure 6 is the region of interest and the roughness curve shows the distribution of that region. All the histogram/distribution heights for all the samples are Gaussian, although, the distribution heights are not symmetry due to the skewness at the valleys.

Figure 7 shows the scope trace for scanned sample P37. The dual pattern used represents the trace and the retrace pattern. This is implemented in order to ensure good image capturing.

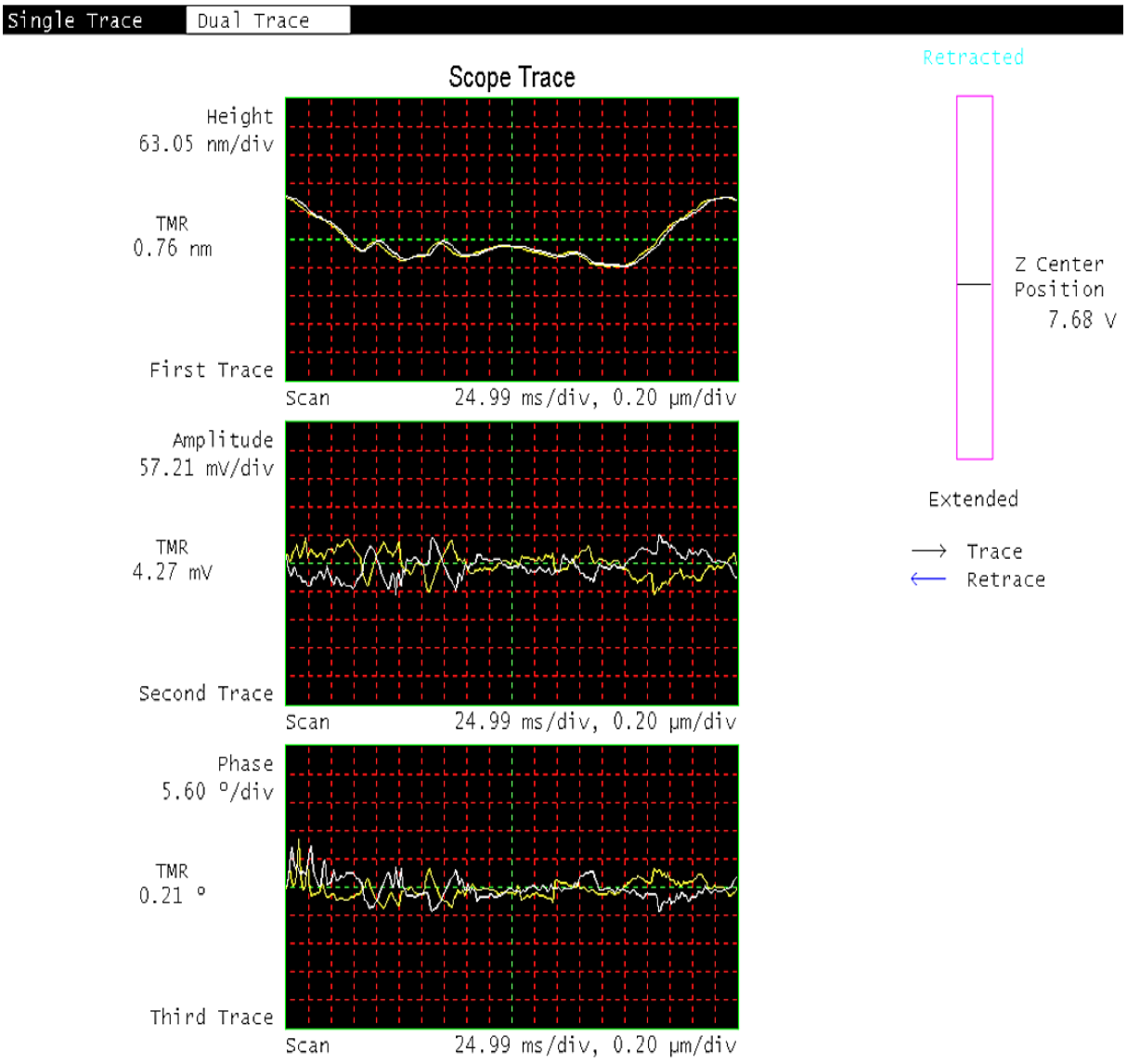

Figure 7. Scope trace for scanned Ti6Al4V/5Cu of sample P37.

The scope trace incorporates the graphs of the heights, amplitudes and phases of the surface topographies. The trace patterns must be approximately equal to the retrace pattern for a good image to be obtained most especially the height in the first trace.

Table 4 illustrates the statistical image result of the sample's surface topography; and highlights the values for the Rms, Ra, Rmax and the surface areas of the samples.

Table 4. Statistical image result of the sample's surface topography

Samples	Rms (nm)	Ra (nm)	Rmax (nm)	Surface Area (μm)^2
P27	99.08	78.60	592.17	12.13
P35	56.53	43.25	354.31	10.29
P36	38.31	31.03	249.22	6.48
P37	48.68	37.64	284.92	16.59

The Root Mean Square (Rms) values, which represent the average profile height deviations from the mean line, were highlighted in the table. Ra values denote the arithmetical average of the absolute values of the profile height from the mean line; while the Rmax values signify the maximum roughness measured from the top of the uppermost crest to the bottom of the lowermost valley. The roughness values for sample P27 of Ti6Al4V/3Cu alloy are higher than those of the other samples. It has the highest Rmax value of approximately less than 600 nm, and the average roughness Ra of approximately 80 nm. The values obtained, as shown in Table 4, show that the surface topographies of all the samples are rough and irregular; and more particularly the 3D view of sample P27 (see Figure 5 (a)).

3.3. Correlation between Wear Loss and Surface Roughness

A correlation between the surface roughness topography and the wear loss of the laser deposited samples was established. Table 5 shows the wear loss estimations for the laser deposited samples.

Table 5. Wear loss estimation

Samples	**Wear scar width W (mm)**	**Stroke length L_k, (mm)**	**Wear depth W_{dt}, (mm)**	**Wear loss W_l, (mm)**
Sample P27	1.323	1.931	0.082	0.236
Sample P35	1.123	1.961	0.071	0.162
Sample P36	1.213	2.105	0.077	0.204
Sample P37	1.125	1.972	0.076	0.175

The wear scar width, stroke length, wear depth as well as the wear loss have been estimated using equations (1) and (2). Sample P27 deposited with a laser power of 1600 W possesses the highest wear loss of 0.236 mm while sample P35 deposited with a laser power of 1200 W possesses the lowest wear loss of 0.162 mm.

Figure 8 shows the relationship between the AFM surface topography and the wear loss.

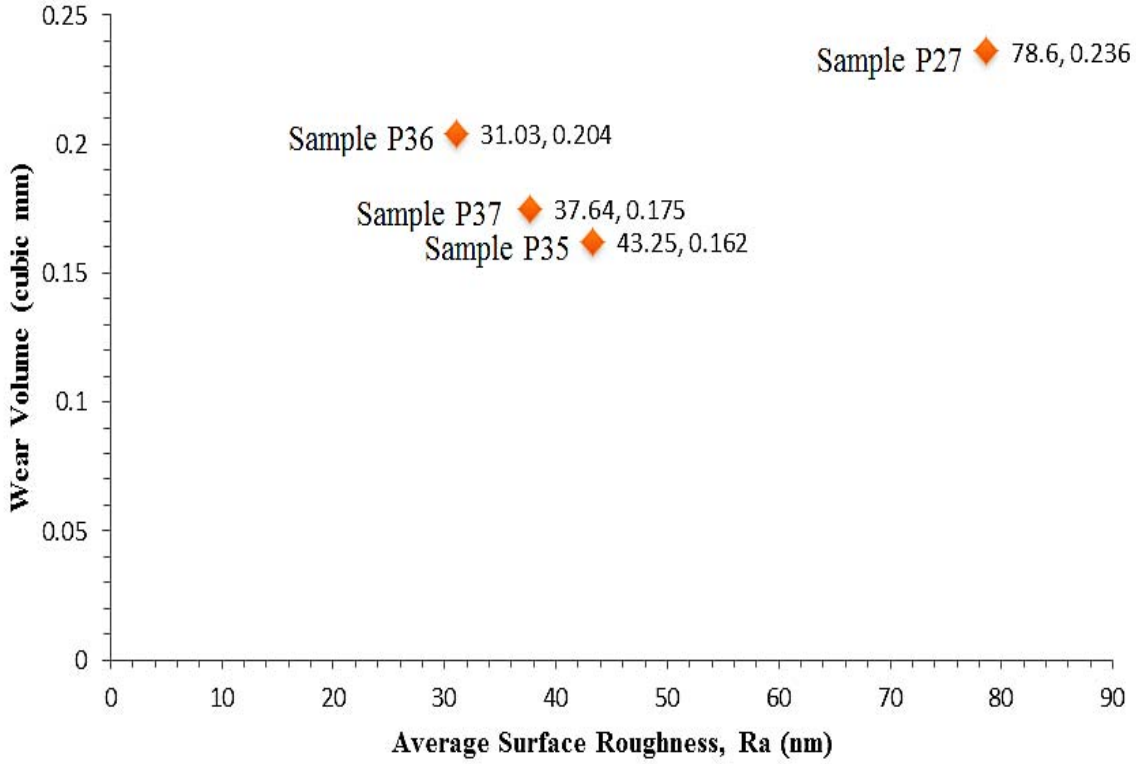

Figure 8. Correlation between the AFM surface topography and the wear loss of the laser deposited samples

The average surface roughness of the samples is inversely proportional to the wear volume/loss. As the surface texture increases, the wear volume decreases. This happens between samples P35, P36 and P37 of Ti6Al4V/5Cu alloys. This was in line with the statement made by Fu et al [32] on the mechanism to improve the wear resistance of a material. From the roughness values obtained between samples P35, P36 and P37, respectively, it can be deduced that the laser power has a significant effect on the surface texture. The roughness value obtained decreases from sample P35 to sample P36 by approximately 16 % and increased in sample P37 by approximately 10 %. A reversed similar case occurred for the wear volume/loss between samples P35, P36 and P37 respectively. Only sample P27 that showed a differ result as compared with other samples in both roughness value and wear loss with a high result. This representation was not in line with the results of other samples. The surface was very rough (see the 2D

view of the amplitude of Figure 5 (c)). The peak and the valley developed on the sample's surface were more pronounced. The powder flow rate used for its deposition also plays an important role in the high roughness value since it's about 10 % higher. In other word, 5 wt % of Cu added in samples P35, P36 and P37 has improved the surface roughness and wear loss of the samples more than the 3 wt % of Cu added in sample P27. Although, other laser depositions formed with 3 wt % of Cu have not been characterized further due to the porosities observed in the samples.

The implication of these results shows that surface roughness is a good predictor of the wear behaviour of a mechanical component. The irregularity in the surface of sample P27 shows that it may not be good marine application because nucleation site can be formed which may lead to corrosion cracking in the corrosive environment. Although all the roughness values Ra obtained were very good since they fell within the roughness number (N3) in the ISO 1302 table.

4. Conclusion

Today, laser has been regarded as an effective technology that is widely used by most of the industries to produce and repair near net shaped components. Titanium and its alloys have been widely used and generally accepted due to its excellent combination of properties. Copper has been added to manipulate and enhance the properties of titanium alloy in this study which has been envisaged for marine application. Widmanstätten structures have been found in almost all the microstructures and advance their coarseness as the laser power increases as a result of the influence of energy density that enormously dissipated into the substrate. The surface topography of the laser deposited Ti6Al4V/Cu alloy was also characterized using the atomic force microscopy. The height, amplitude and the phase shift of the samples are measured. The roughness values of sample P35 of Ti6Al4V/5Cu deposited with a laser power of 1200 W exhibited the lowest wear loss of 0.162 mm and a roughness value Ra of 43.25 nm which can be considered most appropriate for the intended application.

Reference

[1] Global Market Review. http://www.ipmd.net/shop/powder_metallurgy., IPMD 15th edition (**2012-2013**), (Accessed 2014).

[2] C. Y. Yap, C. K. Chua, Z. L. Dong, Z. H. Liu, D. Q. Zhang, L. E. Loh, S. L. Sing, *Applied Physics Reviews*, **2015**, 2(4), 041101.

[3] D. K. Do, P. Li, *Virtual and Physical Prototyping*, **2016**, 11(1), 41-47.

[4] Advanced Manufacturing Crc Limited. Additive Manufacturing Categories Processes and Materials. http://amcrc.com.au/wp-content/uploads/2013/03/additive-manufacturing-categories-processes.pdf. (Accessed 20 May, 2015).

[5] S. L. Sing, J. An, W. Y. Yeong, F. E. Wiria, *Journal of Orthopaedic Research,* **2016**, 34(3), 369-385.

[6] K. D. Kirkham, C. B. Roundy, in *Current technology of laser beam profile measurements. In: Laser beam shaping: theory and techniques*. Second edition, Dickey, F.M. (Ed.). CRC Press, London, **2014**, 464-524.

[7] V. N. Moiseyev, in *Titanium alloys: Russian aircraft and aerospace applications*. CRC Press Taylor & Froes Group, **2006**, 169-180.

[8] G. Lutjering, J. C. Williams, in *Titanium, Engineering Materials and processes*. Springer, Second Edition, **2007**, 1-449.

[9] C. Leyens, M. Peters (Eds.), in *Titanium and Titanium Alloys. Fundamentals and Applications*, Copyright, WILEY-VCH Verlag GmbH & Co. KGaA, Weinheim ISBN: 3-527-30534-3, **2003**, 1-32.

[10] Y. Lu, H. B. Tang, Y. L. Fang, D. Liu, H. M. Wang, *Material Design*, **2012**, 37, 56-63.

[11] I. Sen, K. Gopinath, R. Datta, U. Ramamurty, *Acta Materialia*, **2010**, 58(20), 6799-6809.

[12] A. K. Gogia, T. K. Nandy, K. Muraleedharan, D. Banerjee, *Material Science and Engineering*, A **1992**, 159(1), 73-86.

[13] M. J. Donachie, in *Titanium: A Technical Guide*. ASM International, **2000**.

[14] R. M. Mahamood, E. T. Akinlabi, M. Shukla, S. Pityana, *Proceedings of the International MultiConference of Engineers and Computer Scientists*, 2013, Hong Kong, Vol. II, **2013**.

[15] Y. Xia, S. D. Luo, X. Wu, G. B. Schaffer, M. Qian, *Materials Science & Engineering* A, **2013**, 559, 293-300.

[16] G. Haugstad, *Overview of Atomic Force Microscopy*. www.charfac.umn.edu/instruments/afm_introduction.pdf, **2012**. Accessed 5 March, 2015.

[17] S. Prabhu, B. K. Vinayagam, *Archives of Civil and Mechanical Engineering*, Vol. XI, **2011**,1, 149-170.

[18] K. Kyzioł, L. Kaczmarek, G. Brzezinka, A. Kyzioł, *Chemical Engineering Journal*, **2014**, 240, 516–526.

[19] M. M. Pariona, V. Teleginski, K. Dos Santos, E. L. R. Dos Santos, A. A. Oliveira, C. Lima, R. Riva, *Materials characterization*, **2012**, 74, 64-76.

[20] Structural Alloys Handbook, Battelle's Columbus Laboratories, Columbus, OH, **1982**.

[21] Y. Fu, N. L. Loh, A. W. Batchelor, D. Liu, X. Zhu, J. He, K. Xu, *Surface Coating Technology*, **1998**, 106(2-3), 193-197.

[22] ASTM E3-11, *Standard Guide for Preparation of Metallographic Specimens*, ASTM International, **2011**. (Accessed 2013 from the database).

[23] ASTM E2651-13, *Standard Guide for Powder Particle Size Analysis*, ASTM International Book of Standards, Vol. 14.02 (Accessed 2015).

[24] G133-05, 2014, *Standard Test Method for Linearly Reciprocating Ball-on-Flat Sliding Wear*, ASTM International (Accessed from the lab manual)

[25] J. Qu, J. Truhan, *Wear*, **2006**, 261(7-8), 848-855.

[26] M. F. Erinosho, E. T. Akinlabi, S. Pityana, *4th International conference on Materials Processing and Characterization, Materials Today: Proceedings*, **2015**, 2, 1166-1174.

[27] S. Palanivel, A.K. Dutt, E.J. Faierson, R.S. Mishra, *Material Science and Engineering: A*, **2016**, 654, 39.

[28] M. F. Erinosho, E. T. Akinlabi, S. Pityana, *Advanced Materials Research*, **2014**, 1016, 177-182.

[29] P. Balu, P. Leggett, R. Kovacevic, *Journal of Materials Processing Technology*, **2012**, 212, 1598-1610.

[30] M. N. Ahsan, A. J. Pinkerton, R. J. Moat, J. A. Shackleton, *Materials Science and Engineering,* A, **2011**, 528, 7648-7657.

[31] Summary of Surface Finish Parameters. http://db.materialoptions.com/ASETSDefense/SEDB/EHC_Alts/Tech_Matls_Info/Summary%20of%20Surface%20Finish%20Parameters.pdf. Accessed online, 16, December 2015.

[32] Y. Fu, N. L. Loh, A. W. Batchelor, D. Liu, X. Zhu, J. He, K. Xu, *Surface Coating Technology*, **1998**, 106(2-3), 193-197.

[33] P. J. Ram´On-Torregrosa, M. A. Rodr´Iguez-Valverde, A. Amirfazli, M. A. Cabrerizo-V´Ilchez, *Colloids and Surfaces* A: Physicochem. Eng. Aspects, **2008**, 323, 83-93.

[34] L. Lai, E. A. Irene, *Journal of Vacuum Science and Technology*, B, **1999**, 17, 33-39.